Inorganic Chemistry

Article

pubs.acs.org/IC

Hydrothermal Synthesis, Structure Investigation, and Oxide Ion Conductivity of Mixed Si/Ge-Based Apatite-Type Phases

Henan Li,[†] Tom Baikie,[‡] Stevin S. Pramana,[†] J. Felix Shin,[§] Philip J. Keenan,[§] Peter R. Slater,[§] Frank Brink,[⊥] James Hester,[∥] Tao An,[†] and Tim J. White*[,†]

[†]School of Materials Science and Engineering, Nanyang Technological University, 50 Nanyang Avenue, 639798 Singapore, Singapore

[‡]Energy Research Institute@NTU (ERI@N), Research Technoplaza, Nanyang Technological University, Nanyang Drive, 637553 Singapore, Singapore

[§]School of Chemistry, University of Birmingham, Edgbaston, Birmingham B15 2TT, U.K.

[⊥]Centre for Advanced Microscopy, The Australian National University, R. N. Robertson Building 46, Sullivan's Creek Road, Canberra, Australian Capital Territory 0200, Australia

[∥]Australian Nuclear Science and Technology Organisation (ANSTO), New Illawarra Road, Lucas Heights, New South Wales 2234, Australia

Supporting Information

ABSTRACT: Apatite-type oxides ($[A^I_4][A^{II}_6][(BO_4)_6]O_2$), particularly those of the rare-earth silicate and germanate systems, are among the more promising materials being considered as alternative solid oxide fuel cell electrolytes. Nonstoichiometric lanthanum silicate and germanate apatites display pure ionic conductivities exceeding those of yttria-stabilized zirconia at moderate temperatures (500−700 °C). In this study, mixed Si/Ge-based apatites were prepared by hydrothermal synthesis under mild conditions rather than the conventional solid-state method at high temperatures. Single-phase and highly crystalline nanosized apatite powders were obtained with the morphology changing across the series from spheres for the Si-based end member to hexagonal rods for the Ge-based end member. Powder X-ray and neutron analysis found all of these apatites to be hexagonal ($P6_3/m$). Quantitative X-ray microanalysis established the partial (<15 at%) substitution of La^{3+} by Na^+ (introduced from the NaOH hydrothermal reagent), which showed a slight preference to enter the A^I 4f framework position over the A^{II} 6h tunnel site. Moreover, retention of hydroxide (OH^-) was confirmed by IR spectroscopy and thermogravimetric analysis, and these apatites are best described as oxyhydroxyapatites. To prepare dense pellets for conductivity measurements, both conventional heat treatment and spark plasma sintering methods were compared, with the peculiar features of hydrothermally synthesized apatites and the influence of sodium on the ionic conductivity considered.

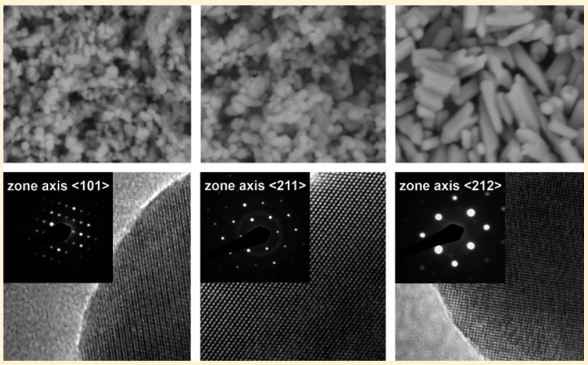

1. INTRODUCTION

Rare-earth silicates and germanates adopting the apatite-type structure have attracted widespread interest as electrolytes for solid oxide fuel cells (SOFCs) because they are superior ionic conductors compared to yttria-stabilized zirconia at moderate temperatures (<700 °C).[1−6] The general formula for the electrolyte oxyapatite is $[A^I_4][A^{II}_6][(BO_4)_6]O_2$, where A is rare earths or alkaline earths and B is Si or Ge. A wide range of chemical substitutions and nonstoichiometry (cation vacancies and/or oxygen excess) can be adjusted to modify ion migration and electrical properties.[7−16] It is well established that the ionic conductivity for A^I cation-deficient phases is significantly higher than that in stoichiometric materials[17−20] and that larger A^{II}/A^I species promote oxygen migration through lower activation energy.[21] Consequently, the larger lanthanum (La^{3+}) apatite analogues usually show superior electrolyte performance, compared to smaller rare-earth (Yb^{3+}) compounds.[22,23]

Apatites are generally $P6_3/m$ hexagonal with an $A^I_4(BO_4)_6$ framework surrounding the $A^{II}_6O_2$ tunnel contents, where the oxygen atoms notionally occupy the center of [001] 1D channels at 0, 0, z (4e according to Wyckoff notation).[21,24] The rare-earth cations (La^{3+}) are located at the (6 + 3)-coordinated A^I position [4f, ($^1/_3$, $^2/_3$, z)] and the A^{II} site [6h, (x, y, $^1/_4$)] bonded to seven oxygen atoms, whereas B cations (Si^{4+}/Ge^{4+}) occupy the 4-coordinated 6h (x, y, $^1/_4$) sites. It is instructive to describe the framework as a motif of A^IO_6 metaprisms that are corner-connected to BO_4 tetrahedra to create adaptive tunnels that expand or contract by tuning the metaprism twist angle (φ).[21,24] Both the framework and tunnel show varying degrees of nonstoichiometry, with cation vacancies concentrated at the framework A^I position. The B site is apparently fully occupied,

Received: September 18, 2013
Published: May 2, 2014

   dx.doi.org/10.1021/ic402370e | Inorg. Chem. 2014, 53, 4803−4812

but coordination to an oxygen atom is variable, with magic-angle-spinning NMR and neutron diffraction revealing BO_5 and BO_6 polyhedra in addition to the BO_4 tetrahedra. In the Ge-containing apatites, these GeO_5 polyhedra serve to accommodate oxygen interstitials necessary for ion migration.[25−28] In the Si-containing apatites, a number of possible sites have been proposed for the location of the oxygen interstitials ranging from the center of the channel to close to the SiO_4 tetrahedra. In addition, B_2O_7 dimers have been suggested as a way to stabilize A^I vacancies.[29]

Apatite electrolytes are mostly obtained at high temperatures (>800 °C) through calcination of homogeneous precursor powders prepared by grinding oxides or sol−gel methods.[1,30] The synthesis of Ge-containing apatites is somewhat problematic, compared to silicates, because of Ge volatilization leading to mixed-phase products.[9,31−34] Recently, a mild hydrothermal synthesis of silicate oxyhydroxyapatites was found to deliver a pure and highly crystalline product at low temperature (230 °C).[35,36] To date, however, there is a lack of systematic studies to establish the optimal hydrothermal conditions for silicate apatite preparation, and analogous germanates have not been produced in this way. Here, we targeted mixed Si/Ge-based lanthanide apatites of composition $La_{9.33}Si_{6-x}Ge_xO_{26}$, for hydrothermal synthesis, with subsequent studies of the crystal chemistry, defect concentration, and powder morphology used to explore the relationship between the structure and ionic conductivity. It was found that germanate apatites are superior electrolyte materials, but for hydrothermally prepared materials, care is needed to control sodium contamination, which lowers the total oxide ion content, and hence also the conductivity.

2. EXPERIMENTAL METHODS

2.1. Synthesis. Apatites of nominal composition $La_{9.33}\square_{0.67}Si_{6-x}Ge_xO_{26}$ (□ represents A^I vacancies, $0 \le x \le 6$) were hydrothermally synthesized from gels with the chemical composition (molar ratio) of 2.5−4.1:5.3:19.3:1722 $La_2O_3/(SiO_2 + GeO_2)/Na_2O/H_2O$. The amount of lanthanum was adjusted empirically to obtain single-phase apatites. In a typical synthesis with Si/Ge = 1, 2.13 g of $La(NO_3)_3{\cdot}6H_2O$ (Strem, 99.9%) was dissolved in 13 mL of deionized (DI) water (solution I). Subsequently, 0.16 g of silicic acid (Merck, 99%) and 0.28 g of GeO_2 (Alfa, 99.999%) were dissolved in the base solution containing 1.54 g of NaOH (Schedelco, 99.9%) in 18 mL of DI water (solution II). These stock solutions were combined by introducing solution I to solution II dropwise, with stirring continued for 2 h at ∼70 °C to ensure that a homogeneous gel formed. This mixture was sealed in a 45 mL Teflon-lined stainless steel autoclave and reconnaissance crystallization performed at 180−240 °C from 3 h to 60 days. On the basis of the yield and crystallinity, a static condition of 240 °C/16 h was selected for the bulk synthesis of powders used for powder X-ray (XRD) and neutron diffraction and ionic conductivity tests. After cooling to room temperature, the product was centrifuged, washed with DI water, and dried at 60 °C overnight. The overall ideal reaction can be expressed as

$$9.33La(NO_3)_3{\cdot}6H_2O + (6 - x)SiO_2 + xGeO_2 + 28NaOH \rightarrow La_{9.33}Si_{6-x}Ge_xO_{26} + 28NaNO_3 + 14H_2O + 55.98H_2O \quad \text{where } 0 \le x \le 6 \qquad (1)$$

The situation is not as straightforward as eq 1 suggests because apatites contain several cation acceptor sites, leading to a wide range of substitutional possibilities,[24] and as considered shortly, monovalent Na^+ ions can potentially displace La^{3+}. Both H^+ and OH^- ions could also be incorporated.

2.2. Powder XRD (PXRD). Laboratory PXRD patterns were acquired at room temperature using a Bruker D8 Advance diffractometer fitted with a LynxEye silicon strip detector. Data were accumulated with Cu Kα (λ_{av} = 1.541874 Å) radiation (40 kV, 40 mA), coupled $\theta-2\theta$ geometry over the angular range 10° < 2θ < 130°, and a step size of 0.02° with a counting time of 1 s/step. The specimens were prepared by pressing powders into poly(methyl methacrylate) (PMMA) rings (⌀ = 25 mm). While XRD delivers accurate lattice parameters, the technique is insensitive to oxygen in the lanthanum-rich matrix, and to arrive at more complete crystallographic descriptions, powder neutron diffraction was undertaken using the Echidna[37] (high-resolution powder diffractometer) beamline at ANSTO (Australian Nuclear Science and Technology Organisation), drawing neutrons from the Open Pool Australian Lightwater reactor. A Ge (335) monochromator with 140° takeoff angle yielded a wavelength of 1.622 Å. The samples were contained in vanadium cans (10 mm diameter), and data were collected at ambient temperature over the range of 2θ = 4−164° with a step size of 0.05° for 3 h. In order to gain additional information on the effect of water incorporation and possible loss at elevated temperature, the silicate and germanate end members were subjected to in situ high-temperature neutron diffraction studies from 25 to 1100 °C.

2.3. Electron Microscopy and Electron Probe Microanalysis (EPMA). For scanning electron microscopy (SEM), secondary electron and backscattered electron images were collected using a JEOL JSM 7600F microscope. The samples were embedded in thermal epoxy resin disks (diameter 25 mm and thickness 5 mm), mirror-polished, and carbon-coated for quantitative analyses, and data were collected at 15 kV and 1 nA using a JEOL JSM 6400 scanning electron microscope equipped with an Oxford Instruments light-element energy-dispersive spectrometer and Link ISIS SEMquant software. To confirm the bulk composition, EPMA was performed for three selected samples on a JEOL JXA-8530F instrument equipped with five wavelength-dispersive spectrometers. The accelerating voltage and current used were 10 kV and 40 nA, respectively. Standards employed were monazite (La) and albite (Na, Si, and Al) minerals obtained from Astimex, while synthetic GeO_2 (Ge) was from Alfa Aesar. The peak counting times for La, Na, Si, Al, and Ge were 30, 60, 30, 60, and 30 s, respectively, and the background counting time was half of the characteristic peak. For transmission electron microscopy (TEM), the apatites were finely ground under ethanol and ultrasonically dispersed for ∼10 min, and then several drops of the suspension were deposited on a holey carbon film supported by a copper grid that was air-dried before introduction to the microscope. High-resolution (HR) images and selected-area electron diffraction (SAED) patterns were collected using a JEOL JEM-2010 instrument operated at 200 keV.

2.4. Fourier Transform Infrared (FTIR) Spectroscopy and Thermogravimetric Analysis (TGA). FTIR spectra of powdered samples suspended in potassium bromide (KBr) pellets were acquired at room temperature from 400 and 4000 cm^{-1} using a Perkin-Elmer (Spectrum 2000) spectrophotometer with a spectral resolution of 4 cm^{-1}. The water contents were assessed through TGA using a Mettler Toledo TGA/SDTA 851 instrument. The experiments were carried out in air with a heating rate of 10 °C/min up to 1000 °C.

2.5. Impedance Spectroscopy. For conductivity measurements, conventional compact pellets (10 mm diameter) were prepared as follows: the apatite powders were mixed with binder (isopropyl alcohol with 3% polyvinyl butyral), pelletized (300 bar) uniaxially, and sintered at 1500 °C for 6 h. Both sides of the pellets were coated with gold paste and then heated to 750 °C to ensure bonding to the pellet. For comparison, spark plasma sintering (SPS),[38−40] a hot-pressing technique with a high heating rate, was applied to fabricate dense [>95% theoretical density (TD)] polycrystalline pellets using a Dr Sinter SPS-825 (SPS Syntex Inc., Japan) apparatus. Apatite powders were loaded into a ⌀ 20 mm graphite die set and uniaxially pressed at a constant pressure of 50 MPa during the entire process. The temperature was first ramped to 600 °C at a rate of 150 °C/min and then to 850 °C at a rate of 100 °C/min. After this rapid heating, the temperature was slowly raised to 950 °C in 3 min, with increments of 50, 30, and 20 °C in each respective minute. The sample was pressed for 5 min at this temperature for the sintering to complete, after which both the pressure and heating power were released for the

dx.doi.org/10.1021/ic402370e | Inorg. Chem. 2014, 53, 4803−4812

samples to cool naturally. Finally, the materials were burned in air at 850 °C for 2 h to remove residual carbon. For both types of pellets, the ionic conductivity was evaluated by alternating-current impedance spectroscopy (Hewlett-Packard 4192A impedance analyzer), with measurements taken in air, with an applied voltage of 0.1 V over a frequency range of 100 Hz to 10 MHz from 300 to 800 °C. The impedance spectra showed a single broad semicircle consistent with a combination of bulk and grain boundary components, and so it was not possible to accurately extract individual bulk resistivities. Consequently, the data reported represent the total conductivities.

3. RESULTS AND DISCUSSION

3.1. Synthesis and Phase Assemblage. Laboratory PXRD patterns confirmed the synthesis of a single-phase

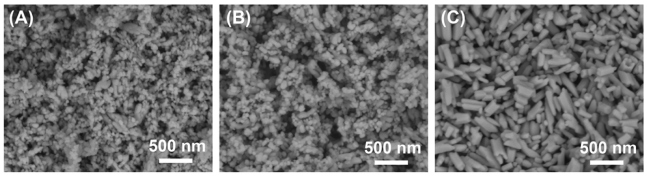

Figure 1. Low-angle backscattered electron micrographs (5.0 kV) for (A) the Si end member, (B) the intermediate composition of nominal equivalent Si/Ge, and (C) the Ge end-member apatites synthesized at 240 °C for 16 h.

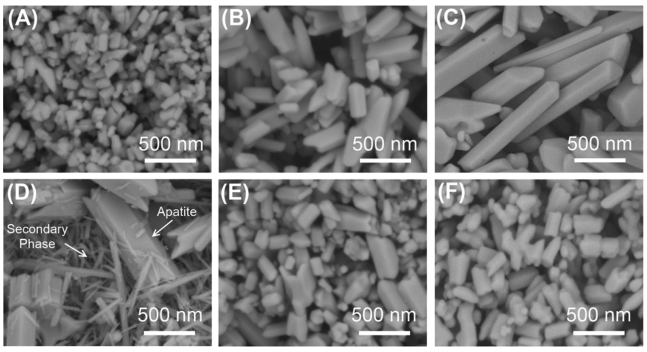

Figure 2. Low-angle backscattered electron micrographs (5.0 kV) for Ge end-member apatites with the following synthesis conditions: (A) 220 °C, 3 h; (B) 220 °C, 6 days; (C) 220 °C, 60 days; (D) 200 °C, 1 day; (E) 220 °C, 1 day; (F) 240 °C, 1 day.

apatite for the Ge end member when the reaction was conducted above 200 °C; for synthesis at 240 °C, the single-phase product formed within 3 h. The Si end member was obtained similarly. On the basis of a fixed ratio of Si/Ge sources and base concentration, the introduced La content was always <85% of the stoichiometric quantity because preliminary experiments found that stoichiometric combinations produce significant amounts of secondary phases [mainly the unreacted $La(OH)_3$], and although longer synthesis times reduced these, they were not eliminated completely even after 60 days of reaction (Figure S1, Supporting Information). Because SiO_2 and GeO_2 dissolve in hot (~80 °C), concentrated NaOH while $La(OH)_3$ precipitates, extrastoichiometric silicon and germanium oxides are required to promote the fast crystallization of apatite. After many trials, it was concluded that, with the La source fixed at 60% of the stoichiometric value, the optimized condition of 240 °C and 16 h produced well-crystallized single-phase apatite across the whole mixed Si/Ge series. These parameters are more robust than reported previously[35,36] (230 °C/6 days), and there remains a degree of flexibility to choose

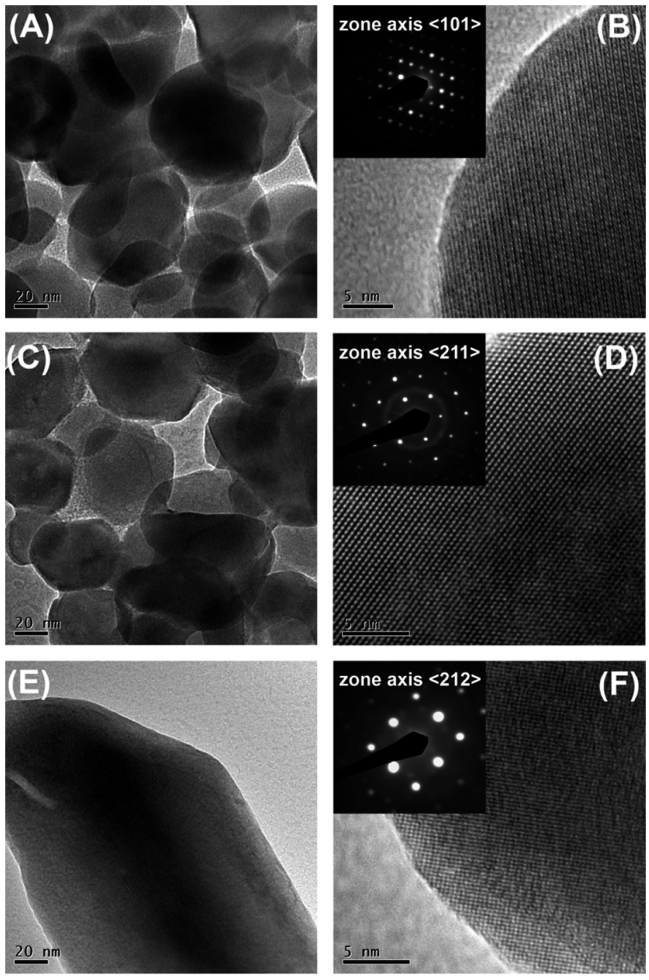

Figure 3. TEM images (low-magnification and high-resolution) and diffraction patterns for (A and B) the Si end member, (C and D) the intermediate composition of nominal equivalent Si/Ge, and (E and F) the Ge end-member apatites.

various combinations of temperature, time, stoichiometry, and reagent-to-water ratio to manipulate the crystal size and morphology.

3.2. Microstructure and Local Structure. Backscattered electron images of the apatite powders found the Si end member composed of spherical nanoparticles (30–100 nm), but as the Ge content increased, the average particle size increased (~40–200 nm) and the spherical crystals elongated, until for the Ge end member the crystals became hexagonal rods (100–600 nm; Figure 1). The microstructures for apatites synthesized under different conditions are collated in Figure 2, and while growth is slow, the rod length increases by an order of magnitude (from 100 nm to several micrometers) after 60 days. Single-phase germanate apatite forms at 220 and 240 °C, but at <200 °C, the large hexagonal apatite rods coexist with acicular $La(OH)_3$.

To confirm that the particles are well-crystallized, SAED and phase contrast imaging were carried out for the two end members and one intermediate composition (x = 3; Figure 3). The microstructures shown in the low-magnification images are consistent with the BEI images. HRTEM contrast was not uniform because rapid damage under the highly energetic electron probe may arise from volatilization of hydrogen-bearing species.

dx.doi.org/10.1021/ic402370e | Inorg. Chem. 2014, 53, 4803–4812

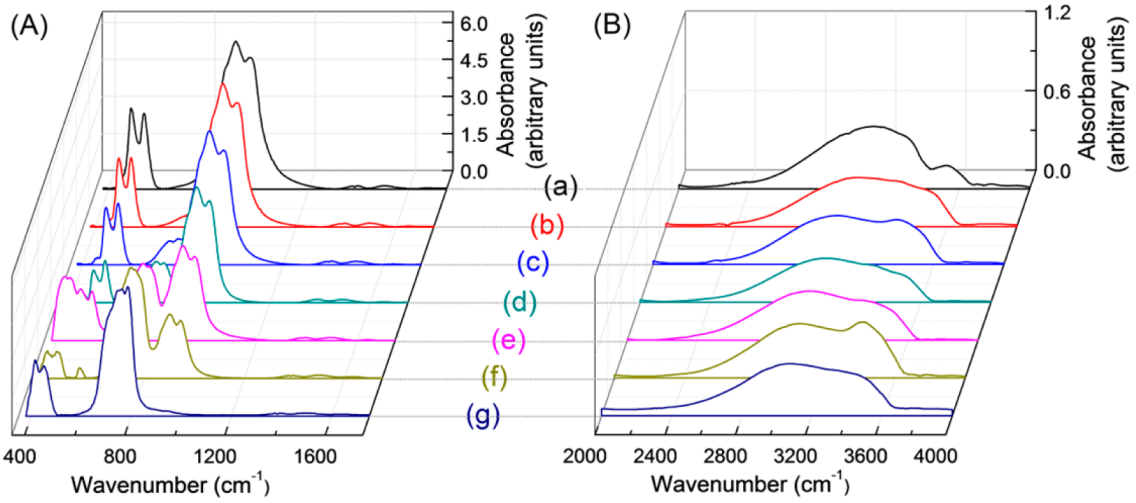

Figure 4. FTIR spectra for mixed Si_{6-x}/Ge_x-based lanthanum apatites with wavenumber ranges of (A) 400−1800 and (B) 2000−4000 cm^{-1}. The intensities were normalized to refined Si or Ge content with (a) Si_6, (b) $Si_{5.82}$, (c) $Si_{5.44}$, (d) $Si_{4.70}$, (e) $Ge_{3.13}$, (f) $Ge_{4.49}$, and (g) $Ge_{5.24}$.

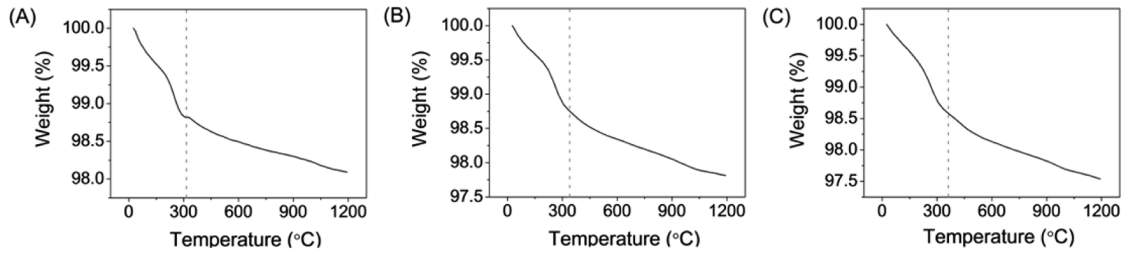

Figure 5. TGA plots for (A) the Si end member, (B) the intermediate composition of nominal equivalent Si/Ge, and (C) the Ge end member apatites synthesized at 240 °C for 16 h.

Table 1. Atomic Ratios for La, Na, and O Scaled to a Total Si + Ge Content of Six Atoms per Formula Unit, Derived from Quantitative EDS and EPMA for Mixed Si_{6-x}/Ge_x Apatites

	La		Na		Si		Ge		O	
nominal x	avg no.	std dev	avg no.	std dev	avg no.	std dev	avg no.	std dev	avg no.	departure from nominal x (%)
$x = 0$	8.14	0.30	1.30	0.06	6.00	0.00	0.00	0.00	24.86	0.0
$x = 0^a$	*8.47*	*0.11*	*1.24*	*0.02*	*6.00*	*0.00*	*0.00*	*0.00*	*25.33*	*0.0*
$x = 1$	8.53	0.39	1.28	0.06	5.76	0.02	0.24	0.02	25.44	76.0
$x = 2$	8.63	0.41	1.17	0.08	5.21	0.03	0.79	0.03	25.53	60.5
$x = 3$	8.62	0.36	1.14	0.05	4.10	0.04	1.90	0.04	25.50	36.7
$x = 3^a$	*8.17*	*0.09*	*1.22*	*0.02*	*4.31*	*0.06*	*1.69*	*0.06*	*24.87*	*43.7*
$x = 4$	8.50	0.39	1.11	0.08	2.76	0.07	3.24	0.07	25.31	19.0
$x = 5$	8.17	0.27	1.05	0.07	1.41	0.03	4.59	0.03	24.78	8.2
$x = 6$	8.28	0.47	1.04	0.04	0.10	0.02	5.90	0.02	24.94	1.7
$x = 6^a$	*8.31*	*0.02*	*1.42*	*0.00*	*0.06*	*0.01*	*5.94*	*0.01*	*25.18*	*1.0*

[a]EPMA.

3.3. Hydroxyl Incorporation: FTIR Spectroscopy and TGA. The FTIR transmission spectra across the Si/Ge series (Figure 4) contain a broad band from 2600 to 3700 cm^{-1} arising from hydroxyl groups and water, but distinct from calcium phosphate hydroxyapatite, the O−H bond stretching mode does not appear as a narrow peak[41] at ∼3570 cm^{-1} and the OH librational mode (∼630 cm^{-1}) was not detected. These differences are suggestive of a low OH^- ion content that is consistent with the previous research,[35,36] indicating the coexistence of OH^- and O^{2-} ions and the formation of oxyhydroxyapatites. The bands at 962 and 910 cm^{-1} belong to asymmetric stretching modes of the SiO_4 group, while those at 542 and 490 cm^{-1} result from asymmetric bending modes of the SiO_4 group and La−O vibration modes.[42,43] Analogously, the bands at 786, 764, 451, and 416 cm^{-1} are assigned to the stretching and bending modes of the GeO_4 group but moved to shorter wavenumbers compared to SiO_4.[31] Further evidence of the presence of hydrous species was obtained by TGA (Figure 5) with significant weight losses (∼2%) observed; the initial ∼1.3% weight loss up to 300 °C should be due to evaporation of absorbed and crystalline H_2O, and the subsequent minor loss up to 1200 °C could be caused by the removal of OH groups, accompanied by conversion to oxyapatite.

3.4. Crystal Chemistry. Quantitative microanalyses (Table 1) were performed by SEM−energy-dispersive spectrometry (EDS) and EPMA; aside from establishing the La/Ge/Si

dx.doi.org/10.1021/ic402370e | Inorg. Chem. 2014, 53, 4803−4812

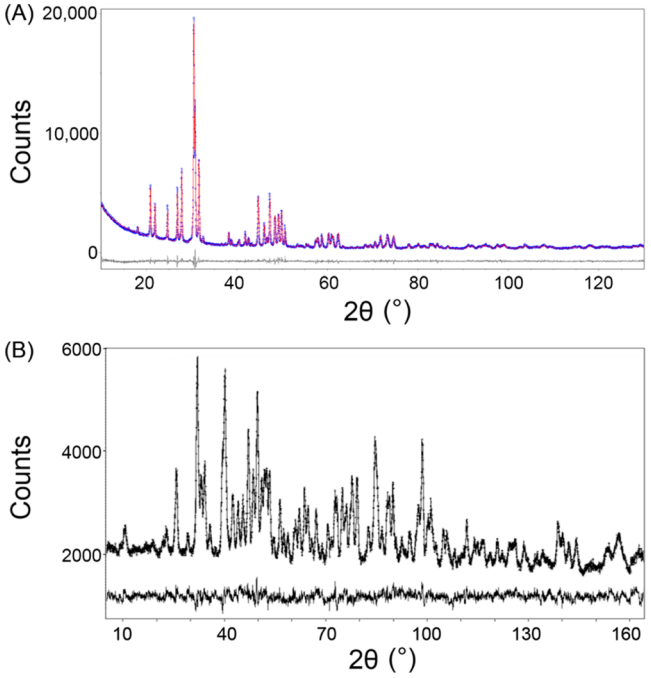

Figure 6. Rietveld plots of the (A) laboratory PXRD and (B) neutron diffraction data of mixed Si_{6-x}/Ge_x-based apatite of nominal $x = 3$ collected at room temperature. The observed intensity is shown by dots, with the solid line representing the calculated intensity. Differences between the observed and calculated intensities are plotted beneath.

content, these analyses were used to investigate the incorporation of Na. There is an apparent deviation from the nominal compositions, which correlates well with the refined compositions from Rietveld analysis. The La content is lower than expected, which is attributed to the incorporation of Na, and through the whole series, the Si/Ge ratio is larger than nominal values. Because both Si and Ge were always in excess with respect to the lanthanum source and the dissolution kinetics of SiO_2[44] and GeO_2[45] are distinct, some departure from nominal product compositions is expected. As the Ge content increases, the Si/Ge ratio approaches its putative value. It is noted that minor Si (<0.2 wt.%) was detected in the Ge end member and is probably introduced by corrosion of glass containers used for the strong alkaline solution. Because of the close characteristic X-ray line energies for Na ($K\alpha_{1,2}$ 1.041 keV), La ($M\alpha_1$ 0.833 keV), and Ge ($L\alpha_{1,2}$ 1.188 keV),[46] the Na contents detected by EDS are potentially inaccurate. However, these characteristic X-rays are readily separated by wavelength-dispersive X-ray analysis (Na = 1.192 nm; La = 1.490 nm; Ge = 1.045 nm), and for confirmation, EPMA on three selected samples (two end members and one mixed Si/Ge of nominal $x = 3$) was performed and the analyses were found to be in reasonable agreement with EDS (Table 1).

Several charge-balanced mechanisms can be formulated to accommodate Na. Because the ionic radii of La^{3+} (CN 6, 1.03 Å) and Na^+ (CN 6, 1.02 Å) are similar,[47] monovalent Na^+ ions may substitute for trivalent La^{3+} by creating oxygen vacancies (eq 2) or occupy La^{3+} cation vacancies together with the incorporation of oxygen interstitials (eq 3).

$$La^{3+} + O^{2-} \rightarrow Na^+ + \square_{O^{2-}} \quad (2)$$

$$2\square_{La^{3+}} + \square_{O_i^{2-}} \rightarrow 2Na^+ + O_i^{2-} \quad (3)$$

A general scheme that includes eqs 2 and 3 can be written as

$$La^{3+} + 2\square_{La^{3+}} \rightarrow 3Na^+ \quad (4)$$

Driven by the charge balancing and characteristics of the synthesis method, it is possible that hydrogen is involved in the form of hydroxide and the valence imbalance caused by Na substitutions could be solved by replacing O with hydroxide ions (eq 5).

$$La^{3+} + 2O^{2-} \rightarrow Na^+ + 2OH^- \quad (5)$$

3.5. Rietveld Refinement and Crystal Structures. The PXRD data were refined with TOPAS[48] and the starting

Table 2. Refined Cell Parameter Data (Hexagonal Cell with Space Group $P6_3/m$) from Laboratory PXRD and Neutron Diffraction on Mixed Si/Ge-Based Lanthanum Apatites

refined composition	unit cell parameters (Å)		volume V (Å^3)	R (%)				GOF
	$a = b$	c		R_p	R_{wp}	R_{exp}	R_b	
X-ray Diffraction								
$La_{8.59}Na_{1.13}Si_6O_{25.45}$	9.72743(10)	7.17977(10)	588.351(14)	3.59	4.57	3.41	1.51	1.34
$La_{8.77}Na_{1.03}Si_{5.80}Ge_{0.20}O_{25.67}$	9.73420(9)	7.18823(9)	589.865(13)	3.40	4.32	3.31	1.45	1.30
$La_{8.97}Na_{0.91}Si_{5.21}Ge_{0.79}O_{25.91}$	9.74885(9)	7.19304(9)	592.038(13)	3.42	4.36	3.29	1.36	1.32
$La_{8.74}Na_{1.02}Si_{4.42}Ge_{1.58}O_{25.62}$	9.78960(15)	7.20219(13)	597.76(2)	4.12	5.39	3.28	1.62	1.64
$La_{8.70}Na_{0.98}Si_{3.22}Ge_{2.78}O_{25.54}$	9.84343(16)	7.21513(14)	605.43(2)	4.44	5.83	3.26	1.65	1.79
$La_{8.64}Na_{1.07}Si_{1.93}Ge_{4.07}O_{25.50}$	9.89589(10)	7.22902(9)	613.083(15)	3.92	5.06	3.23	1.56	1.57
$La_{8.92}Na_{0.92}Si_{0.72}Ge_{5.28}O_{25.84}$	9.93039(6)	7.23768(7)	618.106(10)	3.39	4.40	3.31	1.41	1.33
refined composition	unit cell parameters (Å)		volume V (Å^3)	R (%)				GOF
	$a = b$	c		R_p	R_{wp}	R(obs)	R(all)	
Neutron Diffraction								
$La_{8.42}Na_{1.42}Si_6O_{25.88}H_{0.63}$	9.7272(3)	7.1816(3)	588.48(3)	2.83	3.54	4.14	4.14	1.69
$La_{8.40}Na_{1.54}Si_{5.82}Ge_{0.18}O_{26.12}H_{0.98}$	9.7332(3)	7.1863(3)	589.59(3)	3.15	3.93	4.19	4.19	1.91
$La_{8.59}Na_{1.23}Si_{5.44}Ge_{0.56}O_{25.71}H_{0.63}$	9.7503(2)	7.1955(2)	592.42(3)	3.09	3.85	4.38	4.39	1.86
$La_{8.40}Na_{1.31}Si_{4.70}Ge_{1.30}O_{25.58}H_{0.44}$	9.7912(3)	7.2058(2)	598.26(3)	2.79	3.51	3.90	3.90	1.68
$La_{8.58}Na_{1.17}Si_{2.87}Ge_{3.13}O_{25.62}H_{0.43}$	9.8442(4)	7.2185(2)	605.82(4)	3.13	3.97	4.74	4.74	1.82
$La_{8.46}Na_{1.17}Si_{1.51}Ge_{4.49}O_{26.02}H_{0.96}$	9.8973(3)	7.2309(2)	613.42(3)	3.16	3.93	3.97	3.97	1.72
$La_{8.63}Na_{1.19}Si_{0.76}Ge_{5.24}O_{25.88}H_{1.06}$	9.9451(2)	7.2431(2)	620.40(3)	3.61	4.48	4.26	4.26	1.96

dx.doi.org/10.1021/ic402370e | Inorg. Chem. 2014, 53, 4803−4812

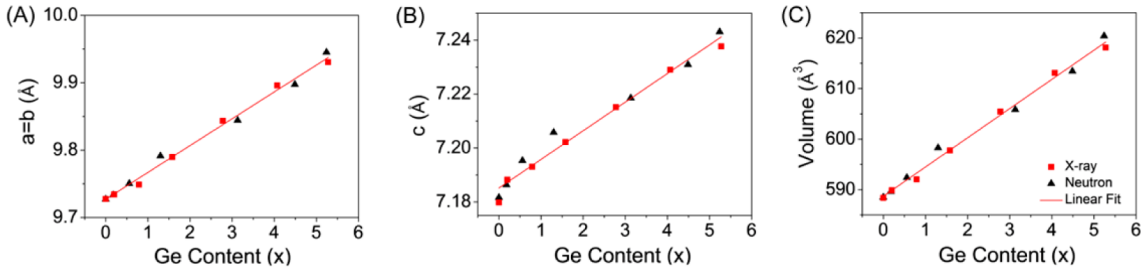

Figure 7. Refined lattice parameters and linear fits from PXRD (squares) and neutron diffraction (triangles) data for the analogue of mixed Si_{6-x}/Ge_x-based lanthanum apatites with refined x from 0 to 6.

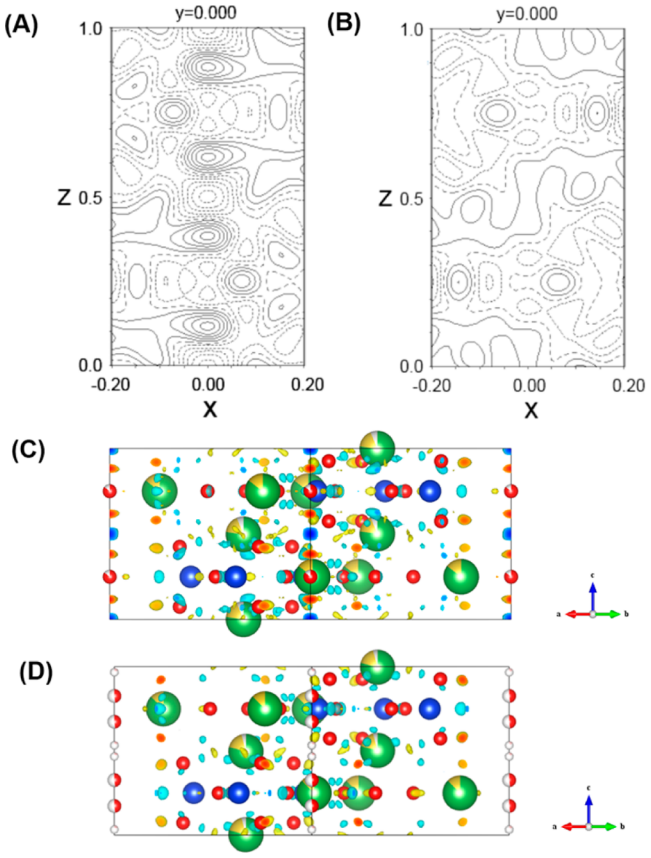

Figure 8. 2D and 3D Fourier mapping for the Si end-member apatite with (A and C) the 2a O position and (B and D) 4e O and H positions.

composition of $La_{9.33}Ge_6O_{26}$ in space group $P6_3/m$ (No. 176). A fundamental parameter peak function was adopted, and the background (four-coefficient Chebychev polynomial and $1/x$ profile), zero error, scale factors, and lattice dimensions were refined sequentially followed by [La/Na] and [Si/Ge] fractional occupancies, atom positions, and isotropic atomic displacement parameters (ADPs). The refinement of neutron diffraction data was conducted with *JANA2006*[49] using the same starting model, but the profile fitting was performed with a pseudo-Voigt peak-shape function and a five-coefficient Chebychev polynomial background, while simultaneously refining the lattice and zero shift parameters. Finally, the occupancies, atom fractional coordinates, and anisotropic ADPs were released simultaneously to complete the crystal structure modeling. In some cases, the tetrahedral O1 and O3 gave nonphysical ADPs, and in these instances, the isotropic displacement parameter was used. Similar observations were made by An et al.[50] and Orera et al.[51] in their analyses of electrolyte apatites, which are believed to be an artifact of tetrahedral disorder.

All of the profiles were satisfactorily modeled in $P6_3/m$ with low R_{wp} values (<6%) for both X-ray and neutron data (Figure 6). The refined lattice parameters (a = b, c) and unit cell volumes dilate linearly with increasing Ge content (x) because Ge^{4+} (CN 4, 0.39 Å) has a larger ionic radius than Si^{4+} (CN 4, 0.26 Å)[47] (Table 2 and Figure 7).

Because the Na^+ ions could reside on both 6h and 4f sites, the occupancies of La^{3+} and Na^+ were allowed to vary, with the constraint of full occupation applied to the 6h [La/Na] site, but not to the 4f [La/Na] site, because vacancies usually appear at the latter position. To maintain neutrality, the substitution of monovalent Na^+ cations on trivalent La^{3+} sites may be balanced by the creation of anionic vacancies. Because the FTIR data indicated the existence of −OH groups, the incorporation of OH^- ions at the expense of O^{2-} ions should also be taken into account. The overall effect makes the expression of the chemical compositions in hydrothermal products rather more

Table 3. Atomic Coordinates and Equivalent Isotropic ADPs for $La_{8.40}Na_{1.31}Si_{4.70}Ge_{1.30}O_{25.58}H_{0.44}$ from Neutron Powder Diffraction

atom	Wyckoff site	x	y	z	SOF	U_{iso} (Å^2)
La/Na2	6h	0.2372(4)	−0.0092(4)	$^1/_4$	0.899(12)/0.101(12)	0.0216(13)
La/Na1	4f	$^1/_3$	$^2/_3$	0.4993(6)	0.753(10)/0.175(13)	0.0154(11)
Si/Ge	6h	0.4033(5)	0.3729(5)	$^1/_4$	0.783(14)/0.217(14)	0.0146(19)
O1	6h	0.3210(5)	0.4859(5)	$^1/_4$	1	0.034(3)
O2	6h	0.5982(5)	0.4713(5)	$^1/_4$	1	0.032(2)
O3	12i	0.3475(4)	0.2566(4)	0.0694(4)	1	0.0441(19)
O4	4e	0	0	0.1873(13)	0.396(10)	0.023(4)
H	4e	0	0	0.03155(6)	0.109(10)	0.02 (fixed)

Space group $P6_3/m$ (No. 176), a = 9.7912(3) Å, c = 7.2058(2) Å, cell volume = 598.26(3) Å^3, and R_{wp} = 3.28%.

dx.doi.org/10.1021/ic402370e | Inorg. Chem. 2014, 53, 4803−4812

Table 4. Anisotropic ADPs for $La_{8.40}Na_{1.31}Si_{4.70}Ge_{1.30}O_{25.58}H_{0.44}$ from Neutron Powder Diffraction

atom	U_{11}	U_{22}	U_{33}	U_{12}	U_{13}	U_{23} (Å^2)
La/Na2	0.0268(16)	0.0267(17)	0.0118(12)	0.0138(13)	0	0
La/Na1	0.0150(13)	0.0150(13)	0.0163(19)	0.0075(7)	0	0
Si/Ge	0.024(2)	0.010(2)	0.012(2)	0.0090(19)	0	0
O1	0.062(3)	0.046(3)	0.019(3)	0.046(3)	0	0
O2	0.036(3)	0.027(2)	0.030(3)	0.015(2)	0	0
O3	0.085(3)	0.040(2)	0.0207(13)	0.041(2)	−0.0230(13)	−0.0001(12)
O4	0.011(3)	0.011(3)	0.046(8)	0.0054(17)	0	0

Table 5. Selected Bond Lengths and Angles for $La_{8.40}Na_{1.31}Si_{4.70}Ge_{1.30}O_{25.58}H_{0.44}$ from Neutron Powder Diffraction

bond	bond length (Å)	bond	bond angle (deg)
La/Na2−O1	2.7684(2)	O1−Si/Ge−O2	114.470(3)
La/Na2−O2	2.4735(2)	O1−Si/Ge−O3	111.0706(16)
La/Na2−O3×2	2.47519(13)	O2−Si/Ge−O3	107.0245(16)
La/Na2−O3×2	2.61183(17)	O3−Si/Ge−O3	105.693(3)
La/Na2−O4	2.41098(14)		
La/Na1−O1×3	2.48200(13)	BVS for La1	2.87
La/Na1−O2×3	2.53867(14)	BVS for Na1	1.06
La/Na1−O3×3	2.8700(3)	BVS for A^I*/valence of A^I*	2.35/2.43
Si/Ge−O1	1.66261(5)	BVS for Si	3.95
Si/Ge−O2	1.65287(14)	BVS for Ge	5.28
Si/Ge−O3×2	1.63272(8)	BVS for B*/valence of B*	4.24/4

*BVSs for A^I and B sites are calculated from the BVS of each element, and the valences for both sites are calculated from the ideal valence of each element: BVS for A^I = BVS_{La} × A^I $occupancy_{La}$ + BVS_{Na} × A^I $occupancy_{Na}$. BVS for B = BVS_{Si} × B $occupancy_{Si}$ + BVS_{Ge} × B $occupancy_{Ge}$. Valence for A^I = 3 × A^I $occupancy_{La}$ + 1 × A^I $occupancy_{Na}$. Valence for B = 4 × B $occupancy_{Si}$ + 4 × B $occupancy_{Ge}$.

Table 6. Conductivity Data for Pellets Prepared from Conventional Sintering and SPS (H0−6 Represent Samples with Nominal x = 0−6, and H0a and H0b Are SPS Samples of the Same Composition but Different Pellet Densities)

	density of pellet (% theoretical)	σ (S·cm^{-1}) at 500 °C	E_a (eV)
Samples Prepared by Conventional Sintering			
H0	68	2.17 × 10^{-7}	1.07
H1	72	2.27 × 10^{-7}	1.08
H2	85	1.74 × 10^{-7}	1.12
H3	79	1.38 × 10^{-7}	1.13
H4	89	3.41 × 10^{-7}	1.12
H5	97	1.60 × 10^{-6}	1.06
H6	95	8.88 × 10^{-6}	1.01
Samples Prepared by SPS			
H0a	96	3.66 × 10^{-5}	0.87
H0b	83	1.30 × 10^{-7}	1.15
H1	98	1.49 × 10^{-5}	0.89
H2	100	1.05 × 10^{-5}	0.88
H3	100	3.93 × 10^{-6}	1.00
H4	99	1.31 × 10^{-6}	1.13
H5	100	8.71 × 10^{-7}	1.12
H6	100	7.43 × 10^{-7}	1.11

complex, compared to solid-state synthesized apatites, and these phases are best described as oxyhydroxyapatites; however, the details cannot be established by XRD. More directly, the 6h [Si/Ge] sites can be regarded as fully tenanted, and the average scattering power of the tetrahedrally coordinated cation is readily determined.

Because neutron diffraction is better able to detect light elements (O and H), this technique was ultimately used for the final structural analysis. To model the tunnel O, the 2a site was initially selected, but Fourier mapping showed a pair of symmetrical excess scattering centers along z (Figure 8A,C), which could be accounted for using a 4e position with a refined occupancy of ≤50%. For all other O positions, full occupancies were appropriate. The remaining negative peaks around the tunnel center (0 0 0) in the Fourier map could be accounted for by placing H^+ ions at these positions (Figure 8B,D). This finding is consistent with the crystal chemistry and the demand for charge balance.

The refined occupancies yielded 2−9% vacancies on the A^I (4f) site. Moreover, the partitioning of Na^+ across A^I (4f) and A^{II} (6h) sites was almost equal, with a slight preference for the A^I framework site (Table 3). The chemical compositions derived from Rietveld analysis were generally consistent with EDS/EPMA chemical analyses. However, the complexity of La/Na/□ and O/OH/□ distributions and occupations mean the chemistries established by Rietveld refinement do not exactly charge balance. Taking the nominal x = 3 as an example, the refined composition is $La_{8.40}Na_{1.31}Si_{4.70}Ge_{1.30}O_{25.58}H_{0.44}$ (overall charge = −0.21), while the charge-balanced expression would be $La_{8.40}Na_{1.31}Si_{4.70}Ge_{1.30}O_{24}(OH)_{2.51-2y}O_y\square_{y-0.51}$. The whole analogue can be represented as $La_{8.50}Na_{1.29}Si_{6-x}Ge_xO_{24}(OH)_{2.79-2y}O_y\square_{y-0.79}$ by taking the average La and Na content of the seven samples.

The ADPs (Table 4) of the channel O atoms (4e) showed significant anisotropy with high U_{33} displacements suggestive of diffusion along the channel or the presence of OH groups displaced off the ideal site to allow for efficient hydrogen bonding to neighboring oxide ions.[52] Large O ADPs are indicative of average scattering of the Si/GeO_4 tetrahedra, as a result of stoichiometric mixing of Si and Ge, together with cooperative relaxation of the BO_4 units that facilitates O ion migration. In addition, the small positive scattering centers inside the tunnels located by Fourier mapping supports the presence of a low concentration of interstitial sites at the channel periphery. This is consistent with previous studies of $La_{9.33}Si_6O_{26}$ that linked these interstitial sites to silicate sublattice distortions. As expected, the smaller Si has a significantly lower bond valence sum (BVS) compared to Ge, while the La^I atom in the metaprism is underbonded and Na is slightly overbonded. The average BVS for A^I and B sites are close to ideal with 2.35/2.43 and 4.24/4 for the composition of $La_{8.40}Na_{1.31}Si_{4.70}Ge_{1.30}O_{25.58}H_{0.44}$ (Table 5).

dx.doi.org/10.1021/ic402370e | Inorg. Chem. 2014, 53, 4803−4812

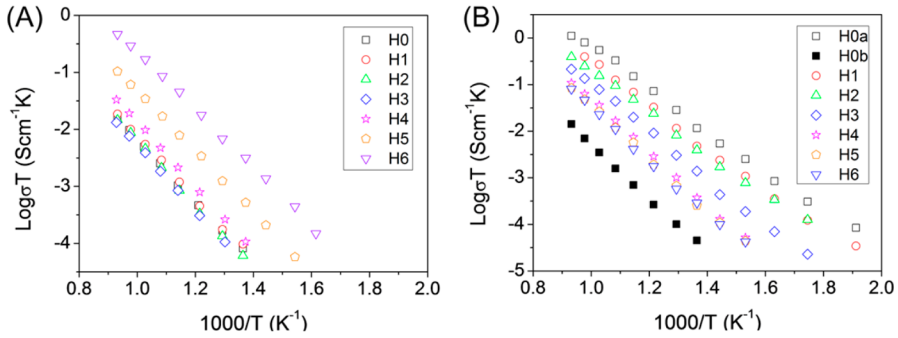

Figure 9. Variation of the conductivities with the temperature for pellets of mixed Si_{6-x}/Ge_x-based lanthanum apatites (H0−6 represent samples with nominal x = 0−6, and H0b is the SPS sample of lower pellet density) prepared from (A) conventional sintering and (B) SPS.

The in situ high-temperature neutron diffraction studies proved the loss of hydroxyl species at elevated temperatures because the profile background, with a significant incoherent scattering component from ^1H, decreases through the whole process (Figure S2, Supporting Information). The major loss was found within 300 °C, which is consistent with the result from TGA. The refined neutron diffraction data collected at 1100 °C showed obvious proton loss and oxygen enrichment (Table S1, Supporting Information), and more free charge carriers could thus be obtained by oxidization of the apatites.

3.6. Oxide Ion Conductivities. Pellets prepared by conventional sintering showed poorer conductivity (Table 6), in line with prior studies of apatite systems, where the comparatively low temperature (particularly for the Si-rich samples) and the short heat treatment (6 h) to limit Ge loss were insufficient for full densification. The recorded conductivities are comparatively low for apatite silicate/germanate electrolytes. Starting from the Si end member, the conductivity does not change appreciably with Ge doping until x = 3, with an obvious increase for $x \geq 4$ that continues to the Ge end member (Figure 9A). This observation can be partly attributed to trends in the pellet density because the silicate-rich electrolytes have lower density (<85% TD) while the germanate-rich electrolytes show significantly improved density (up to 97% TD). A major factor, however, affecting the conductivities is likely to be the incorporation of Na, which has the effect of reducing the cation vacancy and oxide ion interstitial contents, both likely to reduce conductivities.

Slater et al. reported that the conductivity increases with the Ge content only for a single-phase hexagonal apatite, and the optimum Si/Ge ratio for high conductivity was found to be 2/4 in solid-state synthesized $La_{9.33}Si_{6-x}Ge_xO_{26}$ system.[32] In our case, Na substitution for La may play a positive role in maintaining the hexagonal structure and suppressing Ge loss, so the highest conductivity was observed for the Ge-based end member. However, overall the conductivities are lower than those observed from these prior studies, which can be related to the presence of Na reducing both the cation vacancy and interstitial content. The activation energy initially increases with Ge doping and reaches a maximum at Si:Ge = 1:1 and then drops back with further Ge doping, but the absolute change is not large. Because germanate apatites usually have higher activation energies than silicates, the trend observed here for Si-rich samples is accounted for by the low pellet density.

For comparison, pellets of near TD were fabricated using the SPS method. These materials showed significantly improved conductivity for Si-rich apatites, while the conductivity was similar or slightly lower than that of the conventionally sintered pellets for Ge-rich apatites because the density discrepancies were not large (Figure 9B). In terms of the latter, the nanoscaled grain size (Figure S3, Supporting Information) of the SPS pellets may prove negative toward the total conductivity because grain boundary contributions will be more important. The biggest change in the conductivity was for the Si end member (2.17×10^{-7} to 3.66×10^{-5} S·cm^{-1} at 500 °C), matching a higher pellet density (68−96% TD) for conventionally sintered and SPS samples. To confirm the negative effect of porosity, a less dense pellet of the Si end-member apatite (83%) was made by the SPS method and the conductivity dropped by 2 orders of magnitude (Table 6 and Figure 9). For dense pellets composed of micrometer-sized crystals, the bulk conductivity will be intrinsic to the material and independent of the microstructure (e.g., grain size). This may not be true for nanostructured materials, and the grain size will be influential. Therefore, the SPS pellets showed lower conductivity than conventionally sintered samples of similar compaction. Additionally, the conductivity decreases with the Ge content, which is the opposite of conventionally sintered pellets. The corresponding activation energies for Si-rich samples are relatively low (~0.88 eV), while that for Ge-rich samples are much higher (~1.12 eV). As there is no significant difference in the pellet density and grain size across the chemical series, and very minor Ge loss is expected; because SPS does not require long sintering time, the observed conductivity changes through the series are intrinsic and controlled by both the cation vacancies and oxygen defects, with some attenuation of performance arising from the incorporation of Na^+ and possible retention of H^+.

Because the structural studies had indicated the presence of protons in the sample, some measurements were performed in different atmospheres, in particular comparing results in dry and wet N_2. The results indicated a small improvement in the conductivity in wet N_2, which for vacancy conductor systems (e.g., perovskite) can be attributed to a protonic contribution to the conductivity (Figure S4, Supporting Information). However, as described previously,[53] the oxide ion conduction in these apatite systems is mediated by oxide ion interstitials, and the presence of water can lead to the incorporation of both protons and oxide ion interstitials, and so the enhancement in this case could be due to either of these effects.

4. CONCLUSION

Single-phase and highly crystalline Si/Ge lanthanide oxyhydroxyapatite powders were obtained by hydrothermal synthesis. The morphology across the series changes from nanosized spheres for the Si-based end member to hexagonal

dx.doi.org/10.1021/ic402370e | Inorg. Chem. 2014, 53, 4803−4812

rods for the Ge-based end member. EDS and EPMA found limited contamination by Na, while FTIR spectroscopy and TGA proved the hydroxyl incorporation as processing artifacts. The Rietveld refinement was consistent with the $P6_3/m$ structure, and these electrolytes can be represented as $La_{8.50}Na_{1.29}Si_{6-x}Ge_xO_{24}(OH)_{2.79-2y}O_y\square_{y-0.79}$. Overall the conductivities were lower than those of conventionally synthesized systems, which can be related to the presence of Na lowering the cation vacancy and oxide ion interstitial content.

■ ASSOCIATED CONTENT

Supporting Information

Neutron crystallographic data in CIF format for all compositions, PXRD pattern (Figure S1), in situ neutron diffraction analysis (Table S1 and Figure S2), backscattered electron micrographs of the sintered pellets (Figure S3), and impedance spectra in dry and wet environments (Figure S4). This material is available free of charge via the Internet at http://pubs.acs.org.

■ AUTHOR INFORMATION

Corresponding Author

*E-mail: tjwhite@ntu.edu.sg. Tel: +65 6790 4586. Fax: +65 6790 9081.

Notes

The authors declare no competing financial interest.

■ ACKNOWLEDGMENTS

H.L. acknowledges the Nanyang President's Graduate Scholarship provided by Nanyang Technological University. This work was supported by A*STAR (Agency for Science, Technology and Research) SERC Grant 082 101 0021 ("Optimization of Apatite Anion Sublattices in Solid Oxide Fuel Cell Electrolytes"). SPS was performed at the University of New South Wales with the support of Professor Sean Li.

■ REFERENCES

(1) Nakayama, S.; Sakamoto, M. *J. Eur. Ceram. Soc.* **1998**, *18*, 1413.
(2) Nakayama, S.; Sakamoto, M. *J. Mater. Sci. Lett.* **2001**, *20*, 1627.
(3) Higuchi, M.; Masubuchi, Y.; Nakayama, S.; Kikkawa, S.; Kodaira, K. *Solid State Ionics* **2004**, *174*, 73.
(4) Arikawa, H.; Nishiguchi, H.; Ishihara, T.; Takita, Y. *Solid State Ionics* **2000**, *136*−*137*, 31.
(5) Kharton, V. V.; Marques, F. M. B.; Atkinson, A. *Solid State Ionics* **2004**, *174*, 135.
(6) Kuo, Y.-L.; Liang, Y.-Y. *Ceram. Int.* **2012**, *38*, 3955.
(7) Slater, P. R.; Samson, J. E. H. *Diffus. Defect Data, Pt. B* **2003**, *90*−*91*, 195.
(8) Abram, E. J.; Sinclair, D. C.; West, A. R. *J. Mater. Chem.* **2001**, *11*, 1978.
(9) Berastegui, P.; Hull, S.; GarcI GarcI, F. J.; Grins, J. *J. Solid State Chem.* **2002**, *168*, 294.
(10) McFarlane, J.; Barth, S.; Swaffer, M.; Sansom, J. E. H.; Slater, P. R. *Ionics* **2002**, *8*, 149.
(11) Tolchard, J. R.; Sansom, J. E. H.; Islam, M. S.; Slater, P. R. *Ionics* **2004**, *10*, 353.
(12) Tolchard, J. R.; Sansom, J. E. H.; Islam, M. S.; Slater, P. R. *Dalton Trans.* **2005**, 1273.
(13) Tolchard, J. R.; Slater, P. R.; Islam, M. S. *Adv. Funct. Mater.* **2007**, *17*, 2564.
(14) Shaula, A. L.; Kharton, V. V.; Marques, F. M. B. *J. Solid State Chem.* **2005**, *178*, 2050.
(15) Li, H.; Baikie, T.; Pramana, S. S.; Shin, J. F.; Slater, P. R.; Brink, F.; Hester, J.; Wallwork, K.; White, T. J. *J. Mater. Chem.* **2012**, *22*, 2658.
(16) Beaudet-Savignat, S.; Vincent, A.; Lambert, S.; Gervais, F. *J. Mater. Chem.* **2007**, *17*, 2078.
(17) Sansom, J. E. H.; Richings, D.; Slater, P. R. *Solid State Ionics* **2001**, *139*, 205.
(18) Islam, M. S.; Tolchard, J. R.; Slater, P. R. *Chem. Commun.* **2003**, 1486.
(19) Tolchard, J. R.; Islam, M. S.; Slater, P. R. *J. Mater. Chem.* **2003**, *13*, 1956.
(20) Masubuchi, Y.; Higuchi, M.; Takeda, T.; Kikkawa, S. *Solid State Ionics* **2006**, *177*, 263.
(21) White, T. J.; Ferraris, C.; Kim, J.; Madhavi, S. *Rev. Mineral. Geochem.* **2005**, *57*, 307.
(22) Felsche, J. *J. Solid State Chem.* **1972**, *S*, 266.
(23) Sansom, J. E. H.; Kendrick, E.; Tolchard, J. R.; Islam, M. S.; Slater, P. R. *J. Solid State Electrochem.* **2006**, *10*, 562.
(24) White, T. J.; Dong, Z. *Acta Crystallogr., Sect. B: Struct. Sci.* **2003**, *59*, 1.
(25) Pramana, S. S.; Klooster, W. T.; White, T. J. *Acta Crystallogr., Sect. B: Struct. Sci.* **2007**, *63*, 597.
(26) Pramana, S. S.; Klooster, W. T.; White, T. J. *J. Solid State Chem.* **2008**, *181*, 1717.
(27) Pramana, S. S.; Baikie, T.; Kendrick, E.; Schreyer, M. K.; Slater, P. R.; White, T. J. *Solid State Ionics* **2010**, *181*, 1189.
(28) Sansom, J. E. H.; Tolchard, J. R.; Islam, M. S.; Apperley, D.; Slater, P. R. *J. Mater. Chem.* **2006**, *16*, 1410.
(29) Baikie, T.; Pramana, S. S.; Ferraris, C.; Huang, Y.; Kendrick, E.; Knight, K. S.; Ahmad, Z.; White, T. J. *Acta Crystallogr., Sect. B: Struct. Sci.* **2010**, *66*, 1.
(30) Tao, S. W.; Irvine, J. T. S. *Mater. Res. Bull.* **2001**, *36*, 1245.
(31) Sansom, J. E. H.; Hildebrandt, L.; Slater, P. R. *Ionics* **2002**, *8*, 155.
(32) Sansom, J. E. H.; Slater, P. R. *Solid State Ionics* **2004**, *167*, 23.
(33) Serra, R.; Alves, C.; Oliveira, F. A. C.; Marcelo, T.; Mascarenhas, J.; Trindade, B. *Ceram. Int.* **2012**, *38*, 5355.
(34) Kinoshita, T.; Iwata, T.; Béchade, E.; Masson, O.; Julien, I.; Champion, E.; Thomas, P.; Yoshida, H.; Ishizawa, N.; Fukuda, K. *Solid State Ionics* **2010**, *181*, 1024.
(35) Ferdov, S.; Sá Ferreira, R. A.; Lin, Z. *Chem. Mater.* **2006**, *18*, 5958.
(36) Ferdov, S.; Rauwel, P.; Lin, Z.; Ferreira, R. A. S.; Lopes, A. *J. Solid State Chem.* **2010**, *183*, 2726.
(37) Liss, K.-D.; Hunter, B.; Hagen, M.; Noakes, T.; Kennedy, S. *Phys. B: Condens. Matter* **2006**, *385*−*386* (Part 2), 1010.
(38) Munir, Z. A.; Anselmi-Tamburini, U.; Ohyanagi, M. *J. Mater. Sci.* **2006**, *41*, 763.
(39) Hungría, T.; Galy, J.; Castro, A. *Adv. Eng. Mater.* **2009**, *11*, 615.
(40) Galy, J.; Salles, P.; Rozier, P.; Castro, A. *Solid State Ionics* **2006**, *177*, 2897.
(41) Fowler, B. O. *Inorg. Chem.* **1974**, *13*, 194.
(42) Rodríguez-Reyna, E.; Fuentes, A. F.; Maczka, M.; Hanuza, J.; Boulahya, K.; Amador, U. *J. Solid State Chem.* **2006**, *179*, 522.
(43) Kannan, R.; Mohan, S. *Mater. Sci. Eng., B* **2001**, *86*, 113.
(44) Greenwood, N. N.; Earnshaw, A. *Chemistry of the Elements*; Pergamon Press: Oxford, U.K., 1984.
(45) Holleman, A. F.; Wiber, E.; Wiberg, N. *Inorganic Chemistry*; Academic Press: New York, 2001.
(46) *X-ray Data Booklet*; Lawrence Berkeley National Laboratory, University of California—Berkeley: Berkeley, CA, 2001.
(47) Shannon, R. D. *Acta Crystallogr., Sect. A: Cryst. Phys., Diffr., Theor. Gen. Crystallogr.* **1976**, *32*, 751.
(48) *Topas V3.0*; Bruker AXS GmbH: Karlsruhe, Germany, 2003.
(49) Petříček, V.; Dušek, M.; Palatinus, L. *Jana2006: The Crystallographic Computing System*; Institute of Physics: Praha, Czech Republic, 2006.
(50) An, T.; Baikie, T.; Wei, F.; Pramana, S. S.; Schreyer, M. K.; Piltz, R. O.; Shin, J. F.; Wei, J.; Slater, P. R.; White, T. J. *Chem. Mater.* **2013**, *25*, 1109.

(51) Orera, A.; Baikie, T.; Kendrick, E.; Shin, J. F.; Pramana, S.; Smith, R.; White, T. J.; Sanjuan, M. L.; Slater, P. R. *Dalton Trans.* **2011**, *40*, 3903.
(52) Panchmatia, P. M.; Orera, A.; Kendrick, E.; Hanna, J. V.; Smith, M. E.; Slater, P. R.; Islam, M. S. *J. Mater. Chem.* **2010**, *20*, 2766.
(53) Orera, A.; Slater, P. R. *Solid State Ionics* **2010**, *181*, 110.